Chapter 2:

Synthesis & Characterization of Rare Earth Doped La_2O_3: Investigation of Optical, Down conversion and Upconversion Properties

Abstract:

The demand for nanomaterial is increasing day by day due to their wide ranging applications in many areas of science and technology. This has led to a rapid growth of nanotechnology. In this work, a simple route of synthesis for nanoparticles (NP) of La_2O_3 has been attempted. The aloe vera gel assisted precipitation method was used to synthesize NP of undoped as well as doped La_2O_3. Four down conversion compounds 1% Pr^{3+}: La_2O_3, 1%Eu^{3+}: La_2O_3, 1%Tb^{3+}: La_2O_3, & 1%Dy^{3+}: La_2O_3 and six upconversion compounds 4% Yb^{3+} - 1% Er^{3+}: La_2O_3, 12% Yb^{3+} - 2% Er^{3+}: La_2O_3, 4% Yb^{3+} - 1% Ho^{3+}: La_2O_3, 12% Yb^{3+} - 2% Ho^{3+}: La_2O_3, 4% Yb^{3+} - 1% Tm^{3+}: La_2O_3, 12% Yb^{3+} - 2% Tm^{3+}: La_2O_3 were also synthesized by this technique. The aloe vera gel acts as a biosurfactant that controls the particle's growth, thus minimizing the particle's size. The structural, elemental, morphological, optical and photoluminescence characterization was carried out on these samples. The XRD & EDAX analysis reveals that the obtained compounds are in the hexagonal phase with high purity having nano crystallite size. The optical bandgap and refractive index have been calculated using the UV – Visible absorption spectra. The average size of synthesized particles was around 60 nm, with a spherical shape, which was confirmed by SEM analysis.

Keyword: XRD, Aloe vera gel, UV-Visible analysis, PL analysis

Graphical abstract:

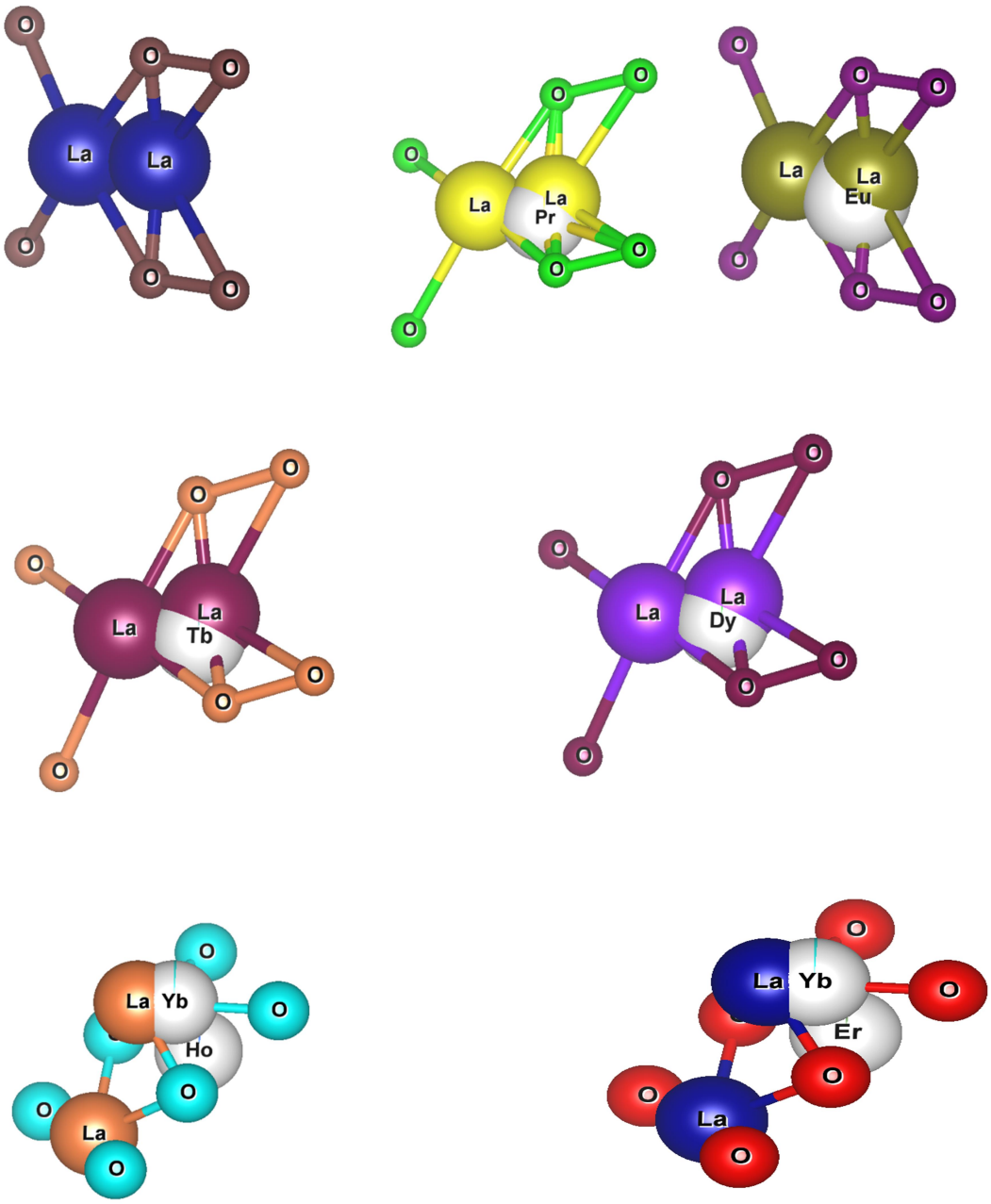

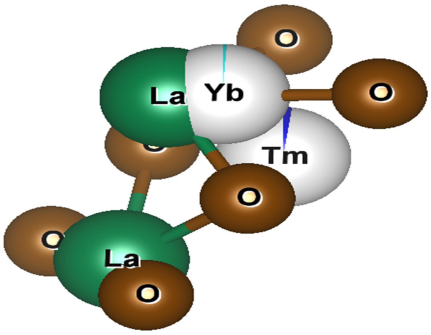
O
La
Yb
O
Tm
O
O
La
O

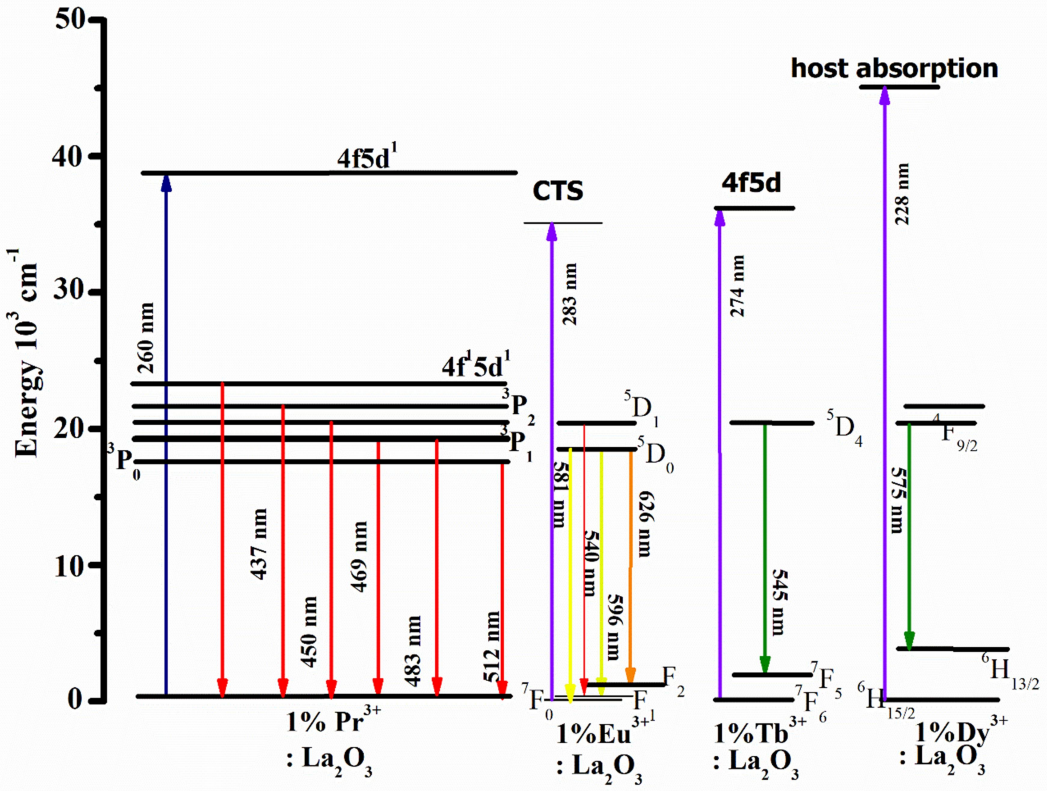
Energy 10^3 cm^{-1}
50
40
30
20
10
0
4f5d^1
4f^{1}5d^1
$^3P_2$
$^3P_1$
$^3P_0$
260 nm
437 nm
450 nm
469 nm
483 nm
512 nm
$^7F_0$
1% Pr^{3+} : La_2O_3
CTS
283 nm
$^5D_1$
$^5D_0$
581 nm
540 nm
596 nm
626 nm
$^7F_2$
$^7F_1$
1%Eu^{3+} : La_2O_3
4f5d
274 nm
$^5D_4$
545 nm
$^7F_5$
$^7F_6$
1%Tb^{3+} : La_2O_3
host absorption
228 nm
$^4F_{9/2}$
575 nm
$^6H_{13/2}$
$^6H_{15/2}$
1%Dy^{3+} : La_2O_3

2.1 Introduction:

The morphology of materials is an important factor that affects the physical and chemical properties of the compounds [1]. As the size of compounds or particles reduces to the nanoscale, the desirable physical properties and chemical properties of the particles are greatly enhanced [2]. This acts as fuel in the rapid growth of nanotechnology. Appropriate synthesis techniques with less complexity and high yield having eco-friendly and cost effective approach are sought. La_2O_3 has applications in many scientific areas such as memory devices[5], sintering additives [6], glass-ceramics [7] [8], super capacitors [9], agriculture [12], catalysis [13], pumping power technology [15], temperature sensor [20], organic light-emitting diodes [21], bio-imaging [22], photo remediation of toxic fast green dye [11], photo catalyst in a monolith photo reactor [16], sensor for hydroquinone chemical [17] and as host in downconversion and upconversion phosphors [10][14][18][19][23].

Several methods have been reported previously for the synthesis of nanoparticles of La_2O_3 such as hydrothermal technique [1], glibulus leaf extract assisted solid-state technique [2], Polyol route [24], Andrographis paniculata leaves extract assisted hydrothermal technique [25], microwave-assisted solution combustion technique[25], reflux routes [2], one-pot combustion synthesis [28] and sol-gel technique [29].

In this work, Aloe Vera gel or Aloe Barbadians Mill assisted precipitation method has been used to synthesize Lanthanum Oxide. The Aloe Vera extract prepared from Aloe Vera leaves, also known as Aloe Vera gel is used as bio surfactant, which helps to minimize the growth of La_2O_3 particles. It is important to use appropriate amount of Aloe Vera gel during the synthesis process due to its strong reducing property. Improper amount of gel can reduce the yield drastically.

2.2 Experimental Procedure:

The experimental process begins with the making of Aloe Vera gel. Mature, healthy and fresh leaves of Aloe Vera were washed with fresh water and dried with a paper towel. The outer green skin layer was removed with a knife. The resulting AV parenchyma (AV gel) was added in distilled water and filtered using a cheese cloth in a vacuum to discard solid residues arising from the cell wall. The clear solution of AV gel was poured into a beaker and stirred on a magnetic stirrer at a temperature of 50°C for 30 minutes. This process led to the solution becoming thicker. This solution of Aloe Vera gel was used in the synthesis process.

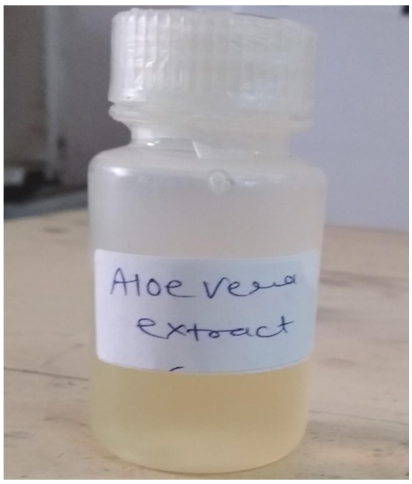

For synthesis of Pristine La_2O_3, stoichiometric amount of $La(NO_3)_36H_2O$ was dissolved in 100 ml de-ionized (DI) water and 20 ml of Aloe Vera gel was added to it. This mixture was poured into a flask and continuously stirred at room temperature on the magnetic stirrer for 2 hours. The pH value was checked at regular intervals. As the pH value reached 3, heat was applied to the solution at a constant temperature of 50°C while adding NaOH drop by drop to turn the solution from acidic to neutral. The formation of precipitates starts on adding NaOH. The neutral solution was filtered using Whatman filter paper. The residues were put in the oven at a constant temperature of 70^0 C. The chunks obtained were crushed into the powder form with the help of mortar and pastel.

The same procedure was applied for the synthesis of four samples of down-conversion materials i.e. 1% Pr^{3+}: La_2O_3, 1% Eu^{3+}: La_2O_3, 1% Tb^{3+}: La_2O_3, 1% Dy^{3+}: La_2O_3 and six samples of up-conversion materials i.e. 4% Yb^{3+} - 1% Er^{3+}: La_2O_3, 12% Yb^{3+} - 2% Er^{3+}: La_2O_3, 4% Yb^{3+} - 1% Ho^{3+}: La_2O_3, 12% Yb^{3+} - 2% Ho^{3+}: La_2O_3, 4% Yb^{3+} - 1% Tm^{3+}: La_2O_3, 12% Yb^{3+} - 2% Tm^{3+}: La_2O_3.

For down conversion materials, the XRD, UV – Visible, SEM - EDAX & Photoluminescence studies were carried out to analyze their structural, morphological, optical & photoluminescence properties.

For upconversion materials, the emphasis was on the study of luminescence properties.

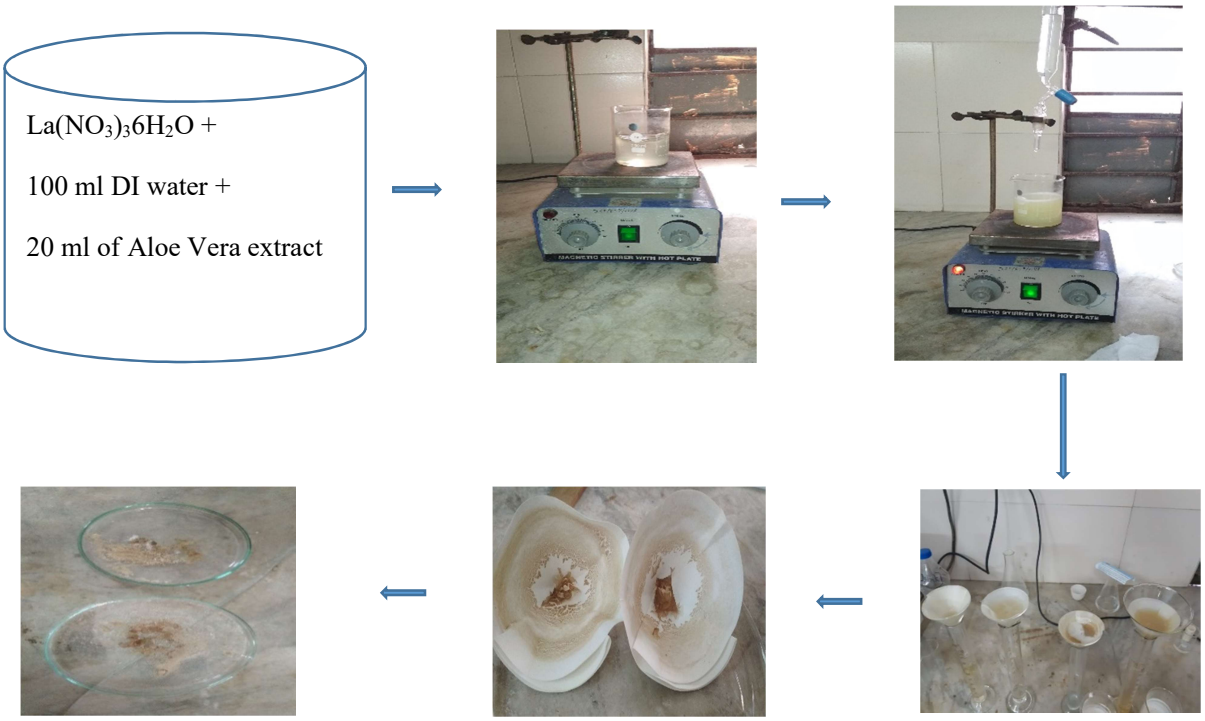

2.3 Results and Analysis of down conversion samples:

2.3.1 Structural, Morphological and Elemental analysis:

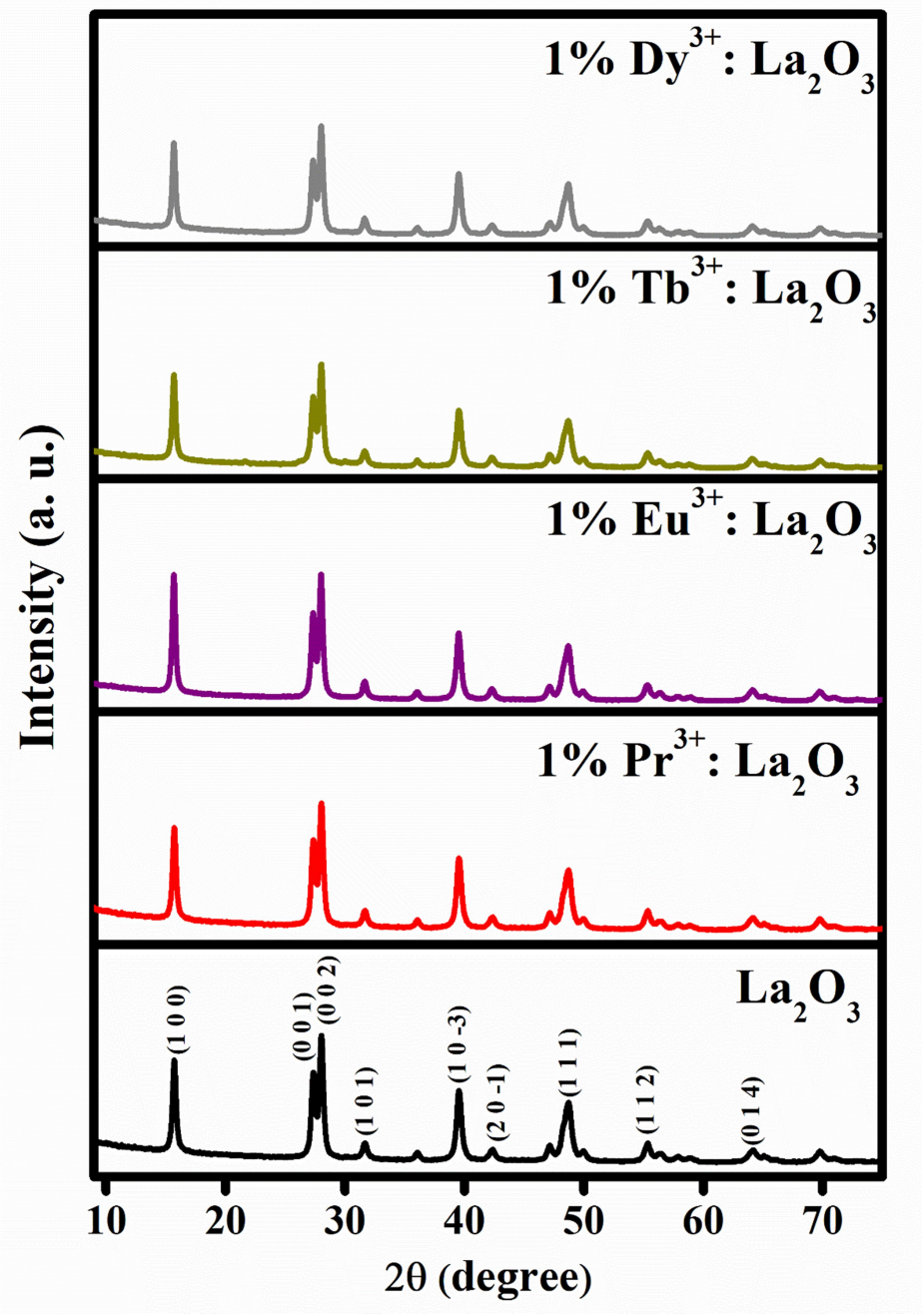

Figure 2.1 XRD of pristine and doped La_2O_3

Synthesized Materials	Phase Name with Space Group	Matching JCPDS file no.	Avg. Crystallite Size (nm)	Lattice Parameters (A°)			Volume $(A°)^3$
				a	b	c	
La_2O_3	Hexagonal $P\bar{6}2m$	83-1344, 83-1345, 40-1279, 40-1281	26.67	6.267	6.267	3.234	109.86
1% Pr^{3+}: La_2O_3			25.22				
1% Eu^{3+}: La_2O_3			22.79				
1% Tb^{3+}: La_2O_3			21.71				
1% Dy^{3+}: La_2O_3			19.64				

Table 2.1 Structural data of doped La_2O_3 samples extracted from the XRD spectra

A Rigaku SmartLab diffractometer operating with Cu K radiation (30 mA, 40 kV) in the 2θ range from 10 to 90°, with the step of 0.02° was used for XRD characterization. Figure 2.1 shows the XRD spectrum of the down conversion samples. The structural data and lattice parameters derived from the XRD pattern (fig.1) are given in table 2.1. The peaks of undoped & doped samples were found to be at the same 2θ values. The peak width varied with the samples. The peaks of the samples were matched with the JCPDS file nos. 83-1344, 83-1345, 40-1279 & 40-1281. All the samples have the hexagonal structure with space group $P\bar{6}2m$. The highest peaks are observed at 2θ values of 15°58' and at 27°39' with the hkl plane (100) and (002). The crystallite size calculated by the Scherrer equation was found to be decreasing in a pattern given by Pr>Eu>Tb>Dy i.e. the dopants. As the pattern of atomic radius is La>Pr>Eu>Tb>Dy, all dopants have an ionic radius less than that of host element Lanthanum. The decrease in crystallite size can be attributed to this factor.

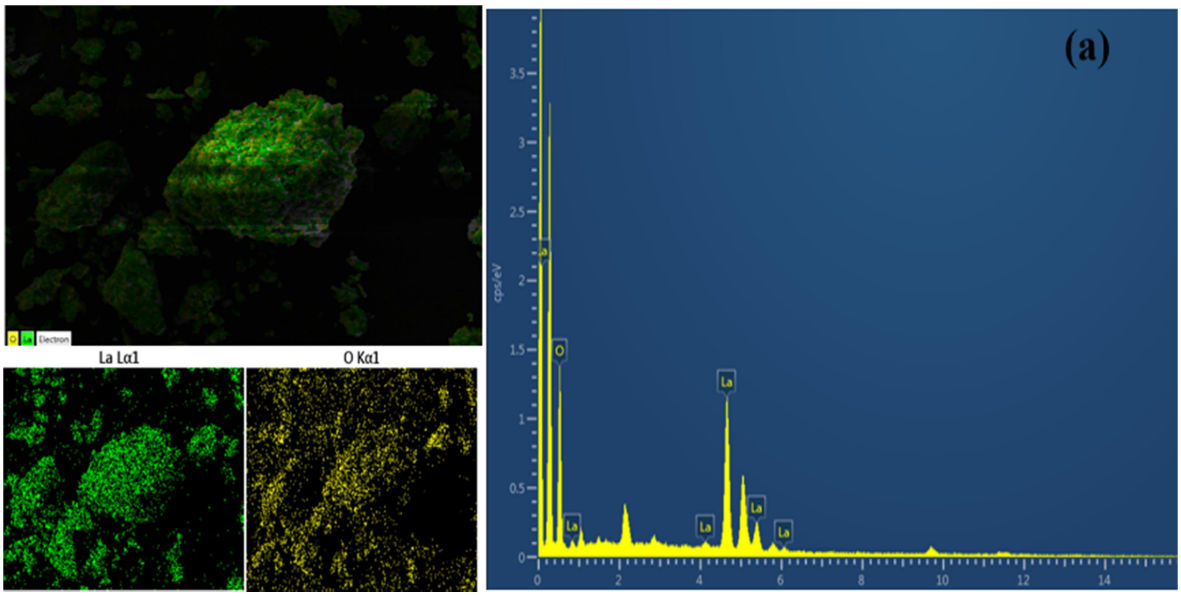

Figure 2.2 (a) EDAX Spectrum with mapping of La_2O_3

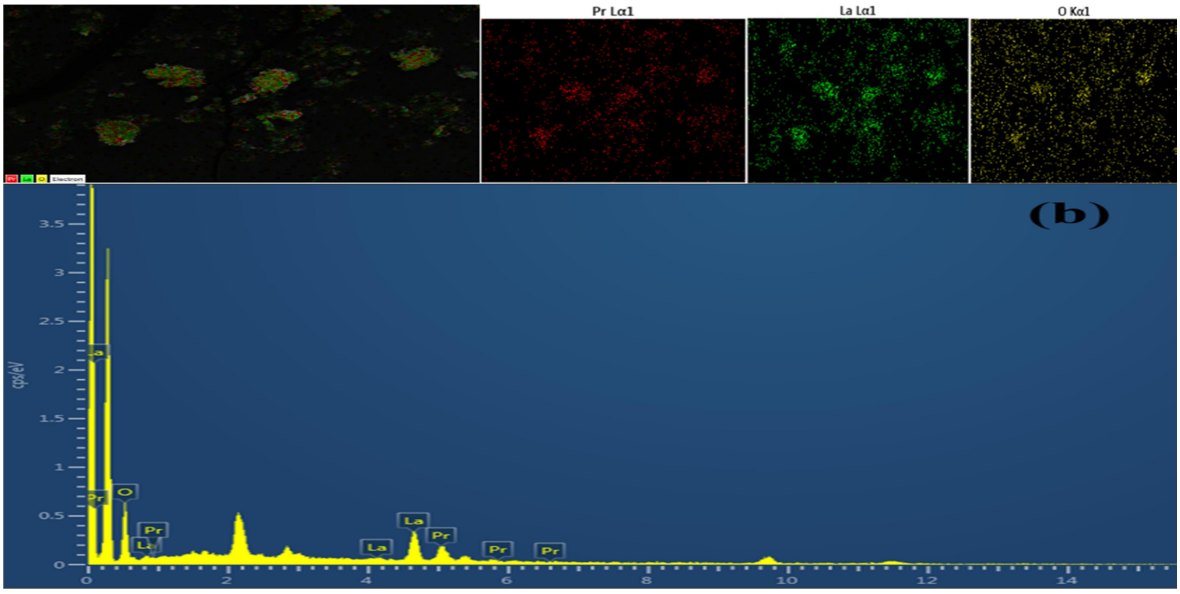

Figure 2.2 (b) EDAX Spectrum with mapping of 1% Pr^{3+}: La_2O_3

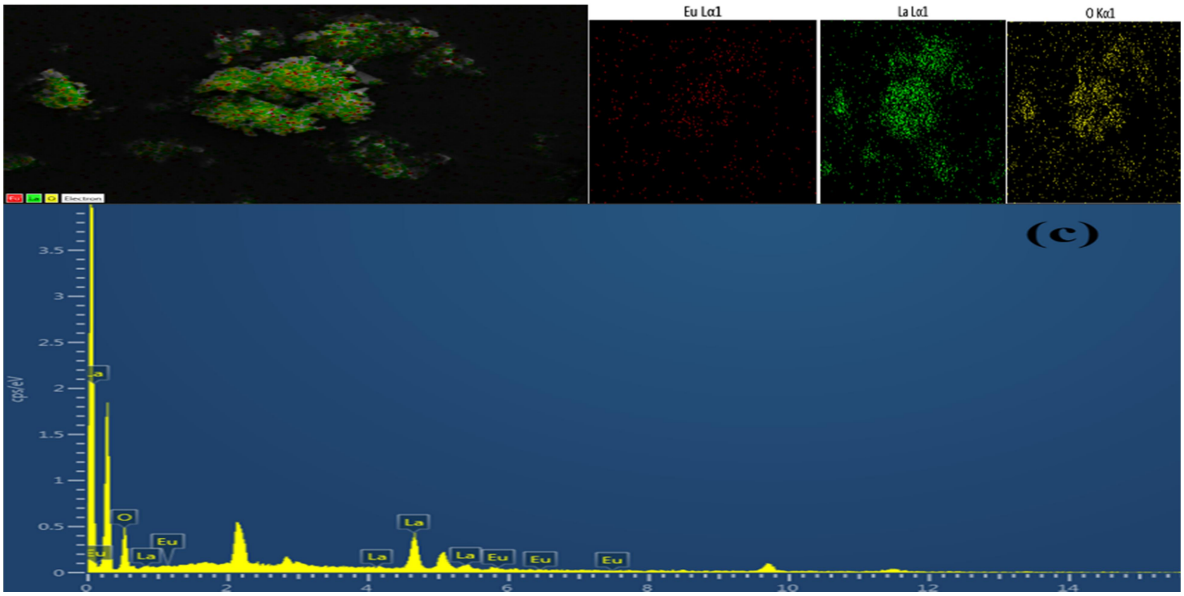

Figure 2.2 (c) EDAX Spectrum with mapping of 1% Eu^{3+}:La_2O_3

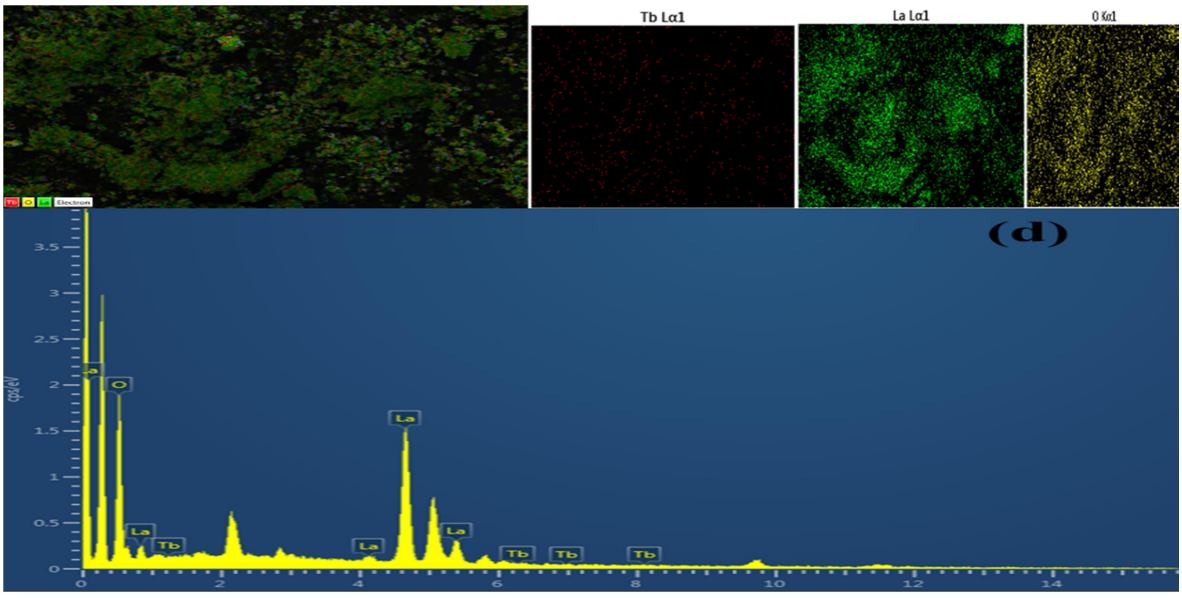

Figure 2.2 (d) EDAX Spectrum with mapping of 1% Tb^{3+}: La_2O_3

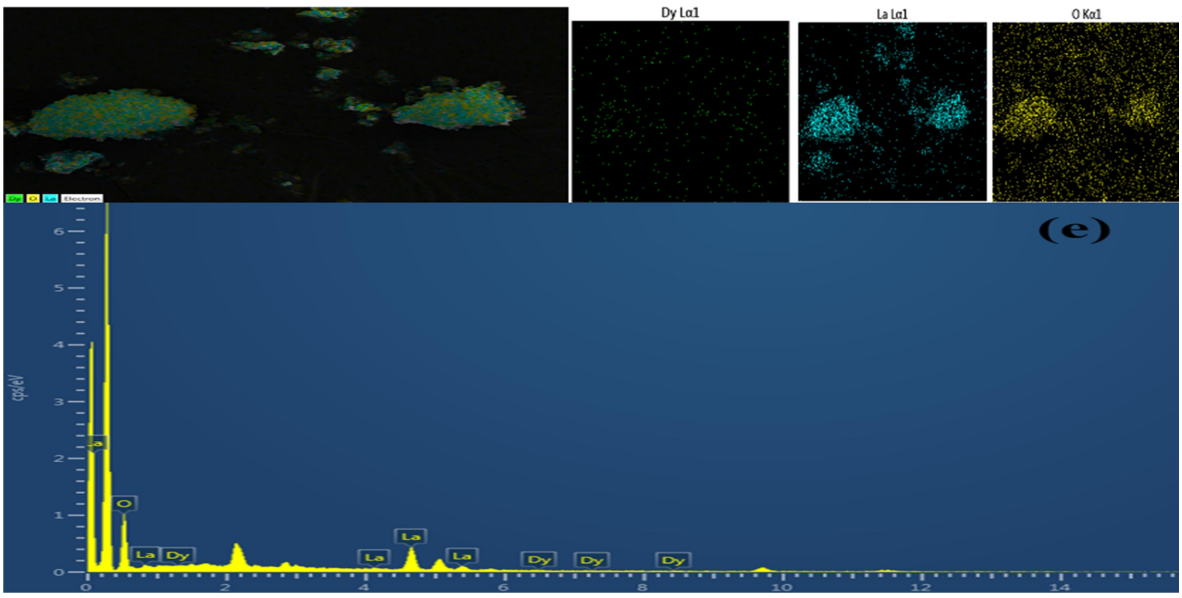

Figure 2.2 (e) EDAX Spectrum with mapping of 1% Dy^{3+}: La_2O_3

Compounds	Elements (Atomic %)					
	La	O	Pr	Eu	Tb	Dy
La_2O_3	38	62	-	-	-	-
La_2O_3: Pr^{3+}	36	62	2	-	-	-
La_2O_3: Eu^{3+}	41	58	-	1	-	-
La_2O_3: Tb^{3+}	43	56	-	-	1	-
La_2O_3: Dy^{3+}	38	60	-	-	-	2

Table 2.2 EDAX data of undoped/doped 1% Ln^{3+}: La_2O_3 with atomic percentage

Fig. 2.2 (a) to (e) shows the EDAX spectrum of La_2O_3 and 1% Ln^{3+}: La_2O_3 along with mapping i. e. the spatial distribution of elements in the sample. This 2D sample section of the sample displays the distribution of elements in the textural context.

The spectrum shows the elemental composition of the material and traces of doped lanthanide ions into the host material. Table 2.2 shows the data extracted from the EDAX spectrum with an atomic percentage in composition and is in conformity with the expected values.

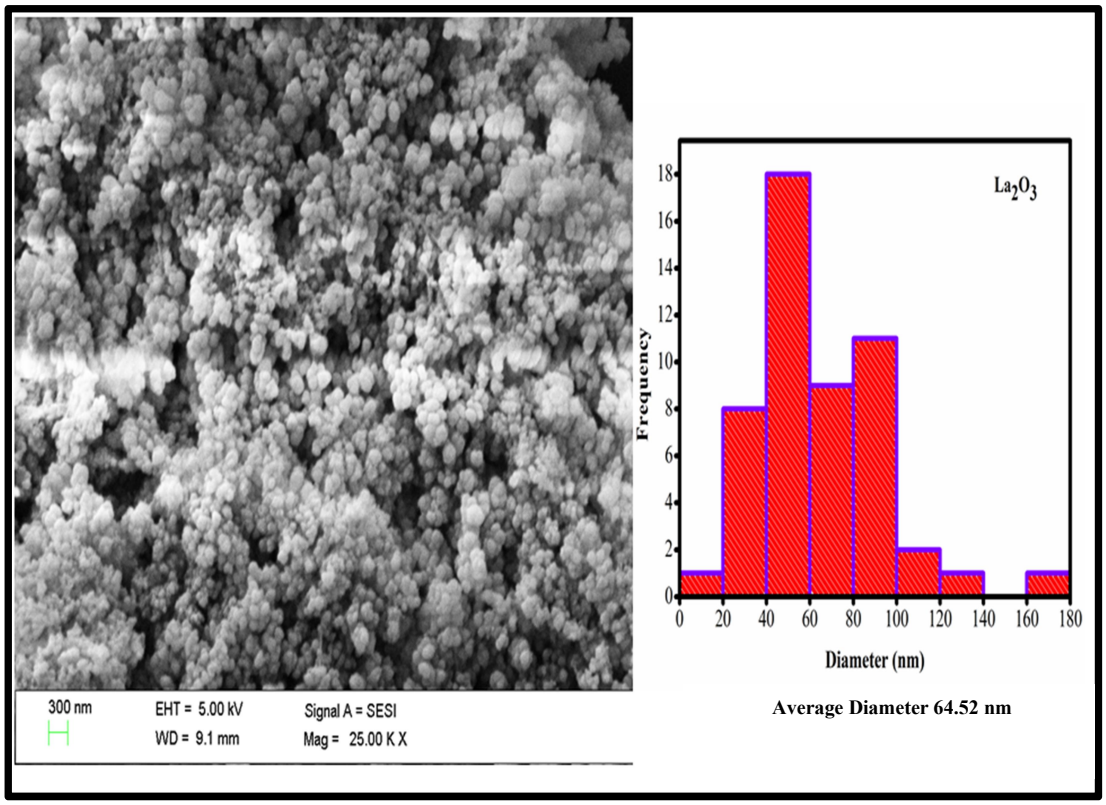

Figure 2.3 (a) SEM image of La_2O_3 with histogram showing particle size distribution

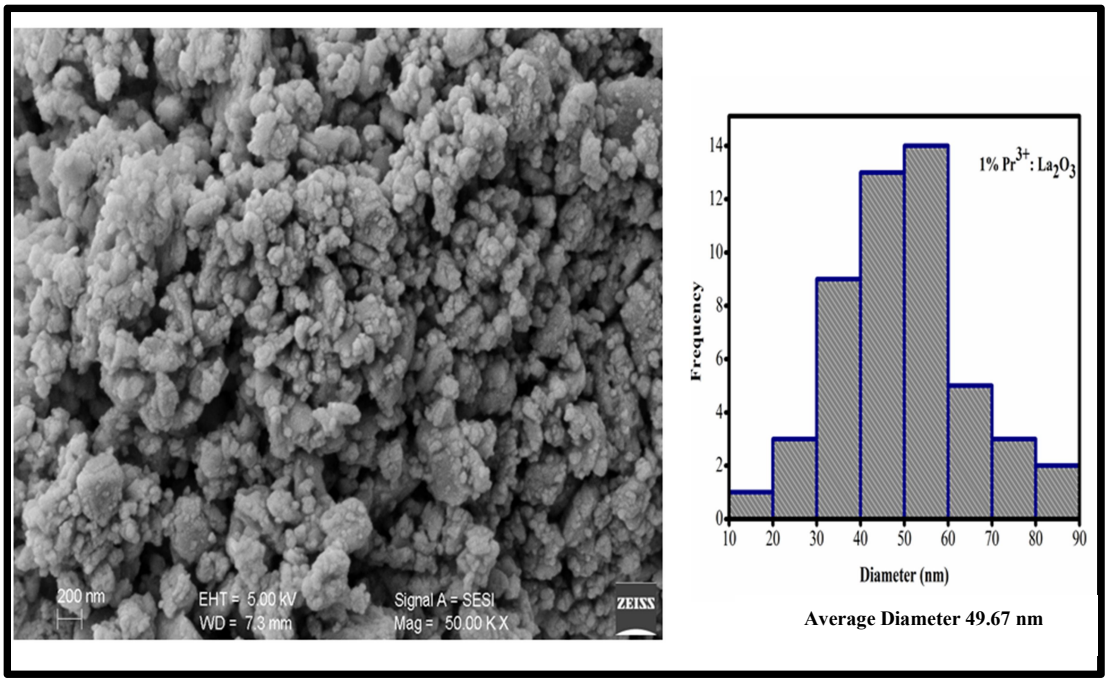

Figure 2.3 (b) SEM image of 1%Pr^{3+}: La_2O_3 with histogram showing particle size distribution

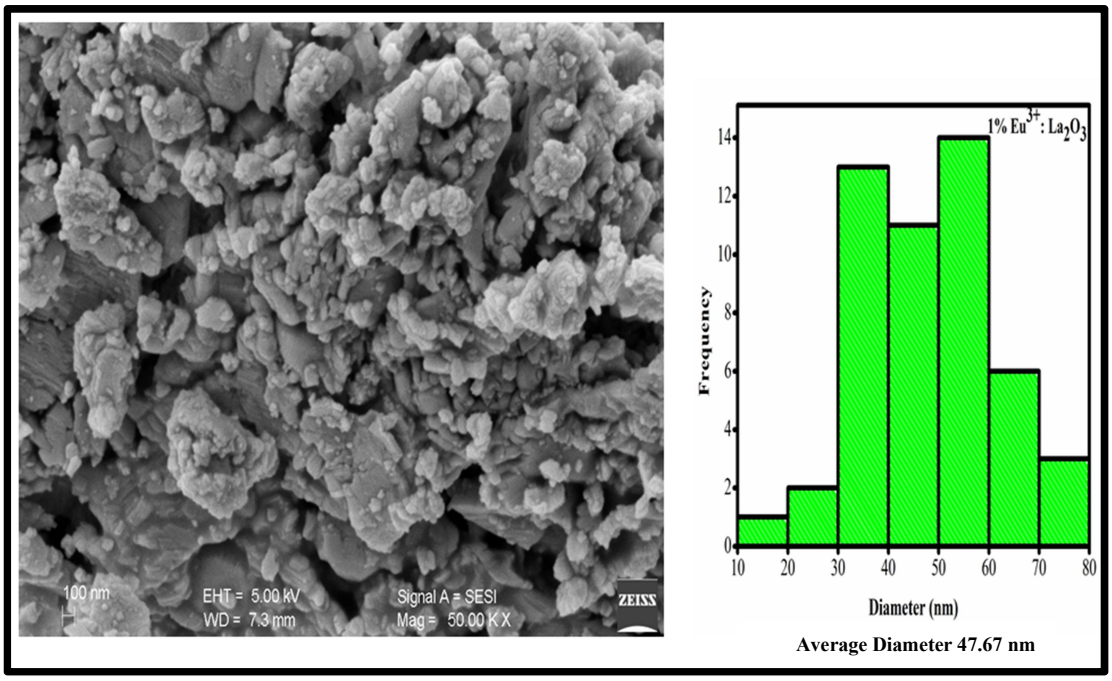

Figure 2.3 (c) SEM image of 1%Eu^{3+}: La_2O_3 with histogram showing particle size distribution

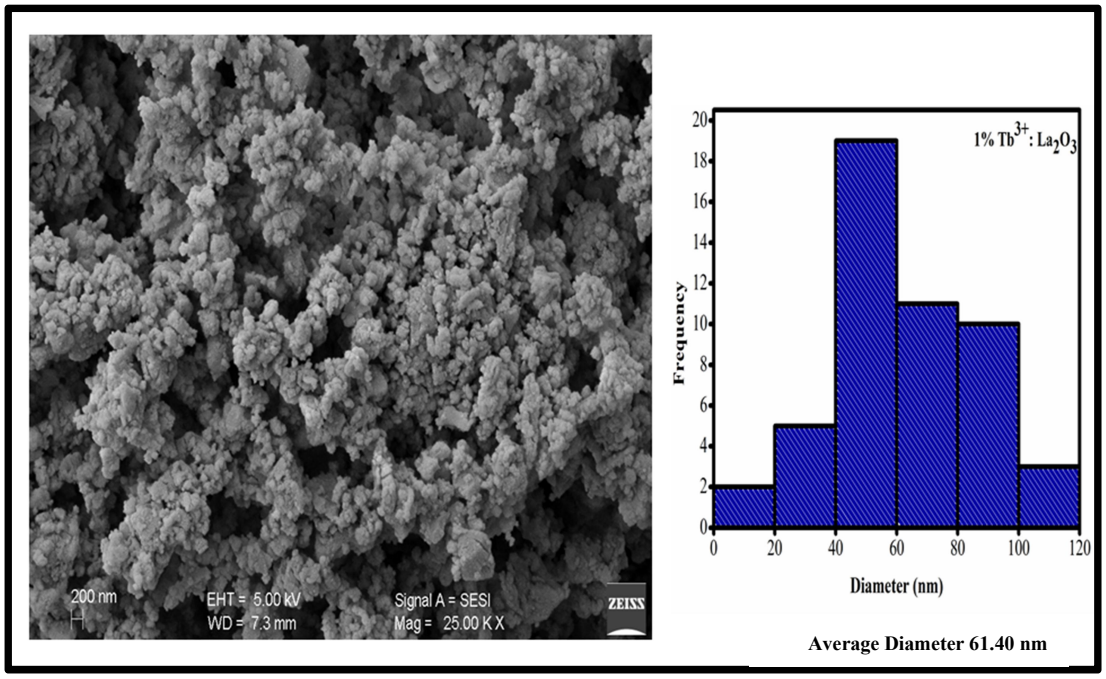

Figure 2.3 (d) SEM image of 1%Tb^{3+}: La_2O_3 with histogram showing particle size distribution

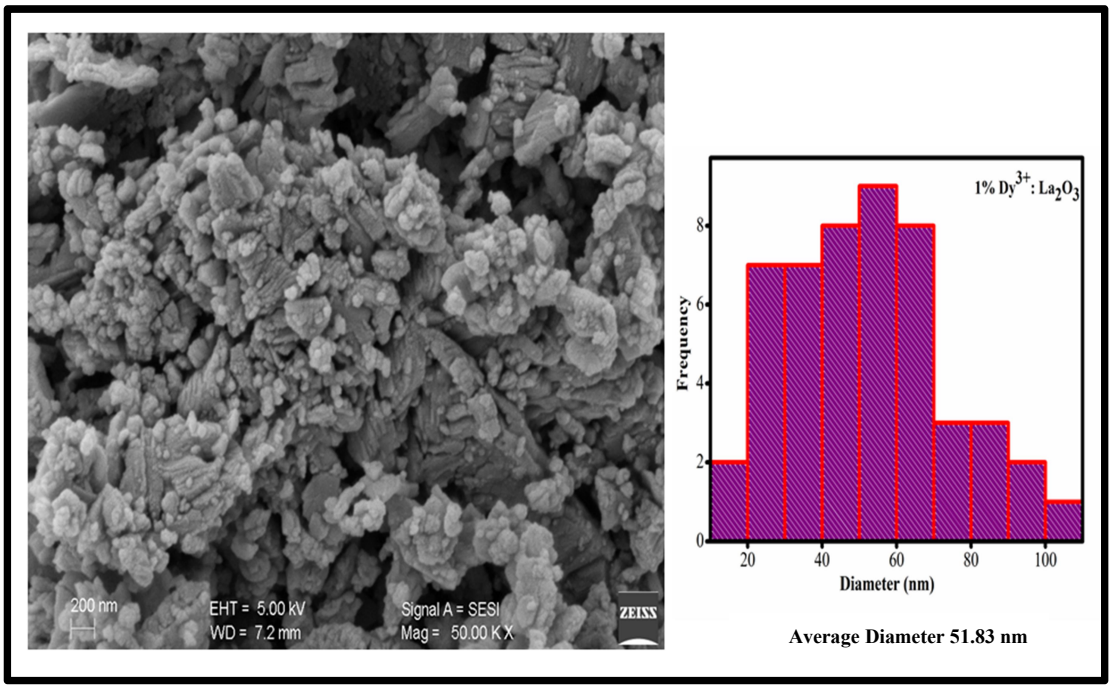

Figure 2.3 (e) SEM image of 1%Dy^{3+}: La_2O_3 with histogram showing particle size distribution

Figures 2.3 (a) to (e) show the SEM images of the samples with histograms giving the particle size distribution in the respective samples. The best images have been chosen for display and analysis. The texture of the samples is identical. The particles are by and large spherical in shape and show aggregation.

The average particle size of synthesized samples is 55 nm.

2.3.2 UV – Visible analysis:

Shimadzu Spectrometer was used for UV-Visible characterization of the samples. 0.05 M aqueous solution was used for the analysis.

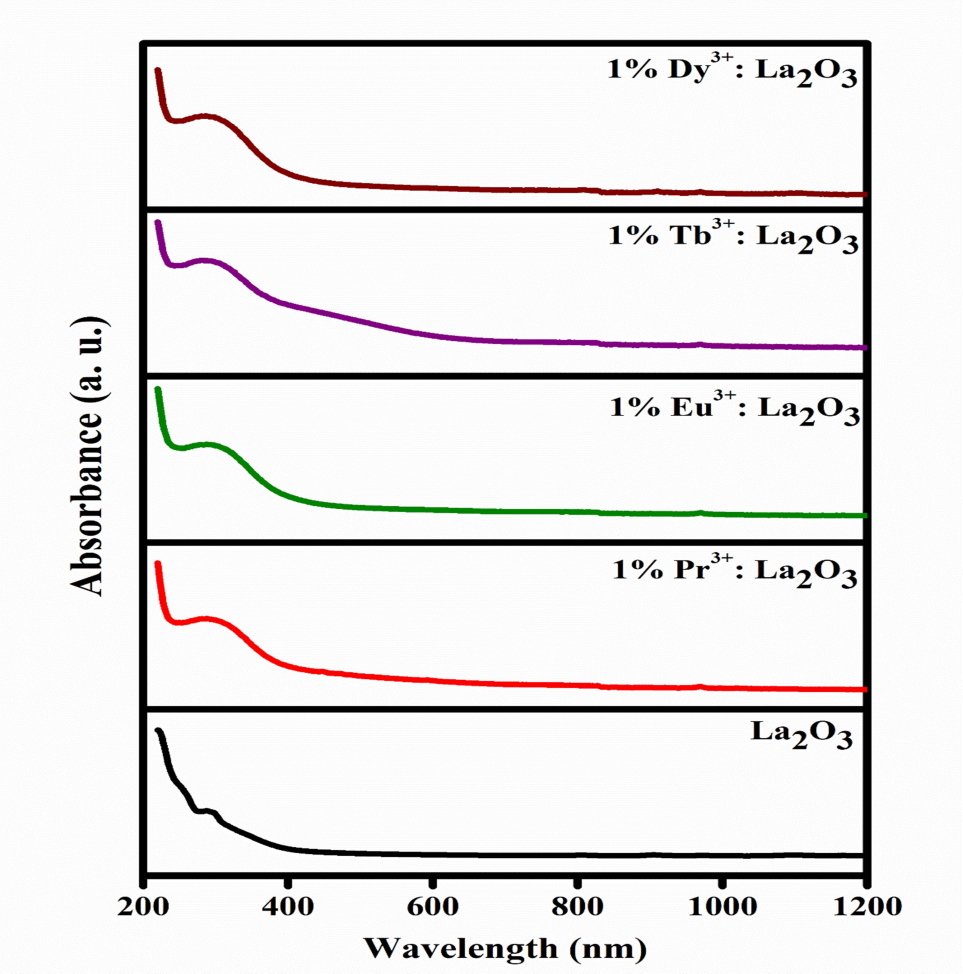

Figure 2.4 UV-Visible graph of 1% Ln^{3+}: La_2O_3

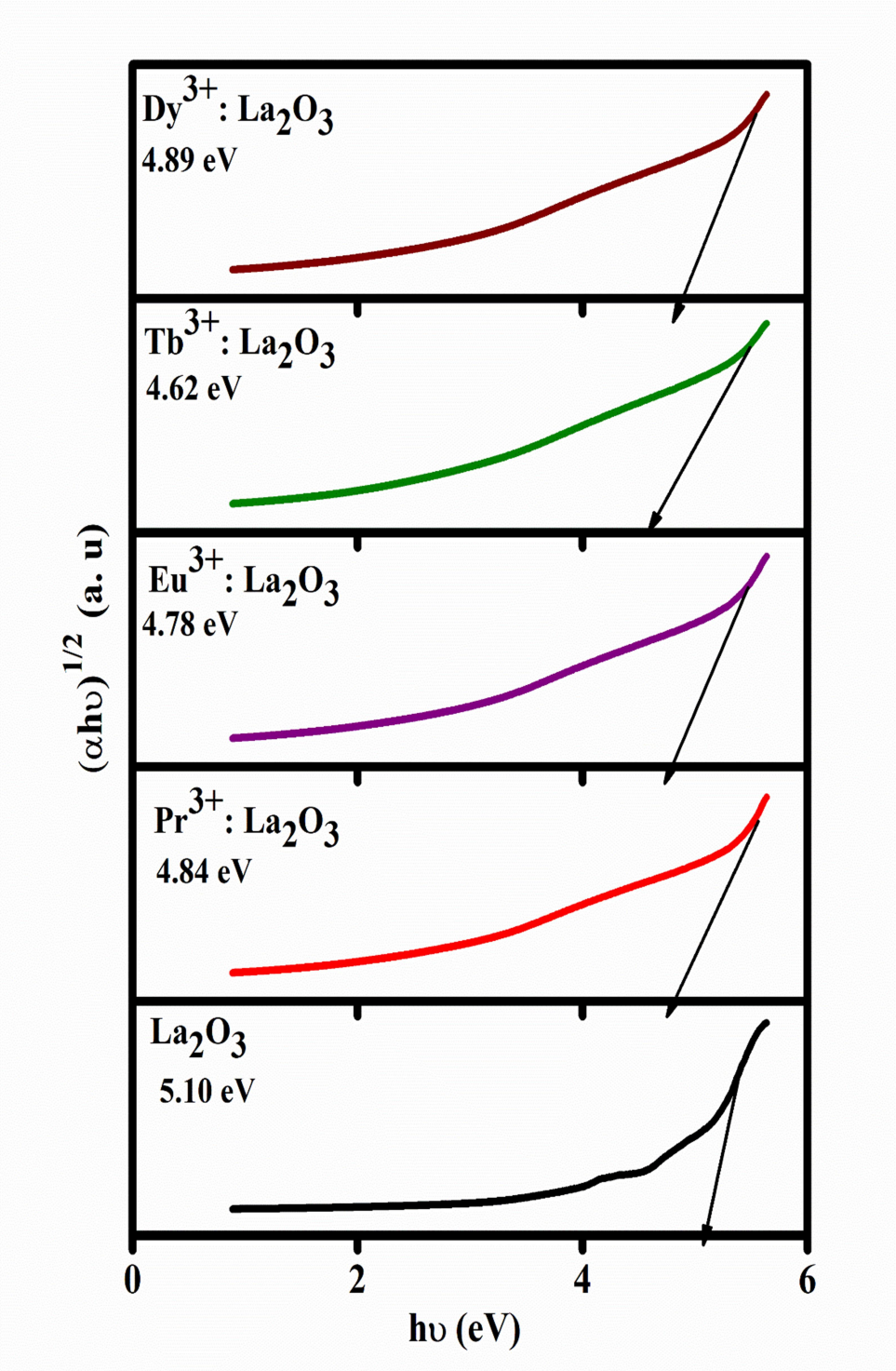

Figure 2.5 Tauc plot Ln^{3+}: La_2O_3

Compounds	λ_{max} (nm)	Band Gap (eV)	Refractive index η
La_2O_3	287	5.10	1.99
1% Pr^{3+}: La_2O_3	288	4.84	2.02
1% Eu^{3+}: La_2O_3	288	4.78	2.03
1% Tb^{3+}: La_2O_3	286	4.62	2.05
1% Dy^{3+}: La_2O_3	286	4.89	2.01

Table 2.3 UV-VIS data of the samples

Fig 2.4 shows the UV—VIS absorbance characteristics of the four samples. Fig 2.5 shows the Tauc's plot to derive the optical band gap. For the optical band calculation, Tauc's plot was used [30],

$$\alpha h\nu = K_1 (h\nu - E_g)^n \quad (1)$$

Equation 1 was Tauc's equation gives the relation between absorption coefficient α and the optical energy band gap E_g. The graph was plotted between $(\alpha h\nu)^{1/n} \rightarrow (h\nu)$ gives the band gap value. Here n = 2 taken for the allowed indirect electronic transition. The refractive index η was calculated from the equation [31],

$$\eta = K E_g^c \quad (2)$$

Where K = 3.3668 & C = -0.32234 were constant & E_g = optical band gap.

Table 2.3 gives the peak wavelength for maximum absorbance, the optical band gap derived from the curves and the refractive index of the material. As shown in fig 2.4, the maximum absorbance of the samples was found to be at wavelengths between 286 nm to 288 nm. The absorption between 2p orbital of O^{-2} and 4f orbital of Ln^{3+} leads to minor changes in the peak

wavelengths. However, there is difference in the absorbance pattern between the doped and undoped samples.

2.3.3 Photoluminescence analysis:

The Photoluminescence excitation and emission spectra were recorded on a Shimadzu make Spectrophotofluorometer.

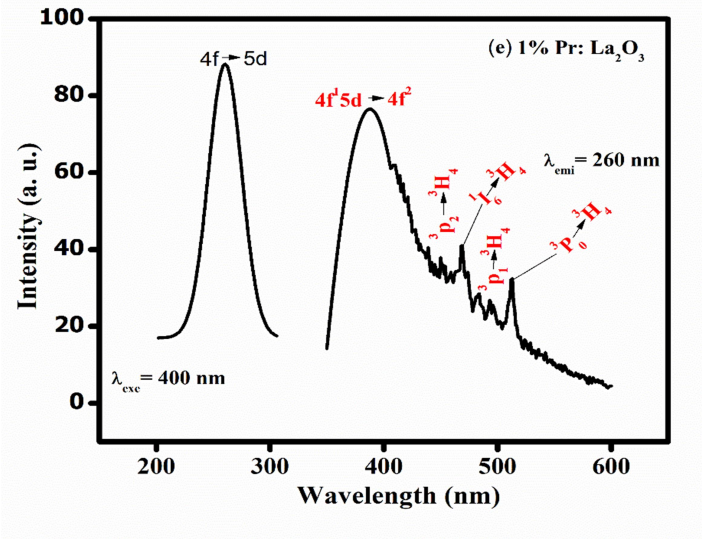

Figure 2.6 (a) Excitation & Emission characteristics of 1%Pr^{3+}: La_2O_3

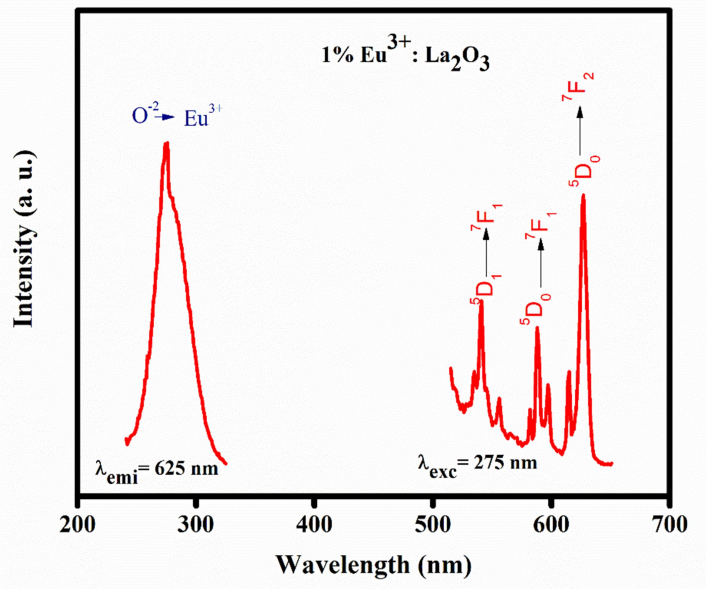

Figure 2.6 (b) Excitation & Emission characteristics of 1%Eu^{3+}: La_2O_3

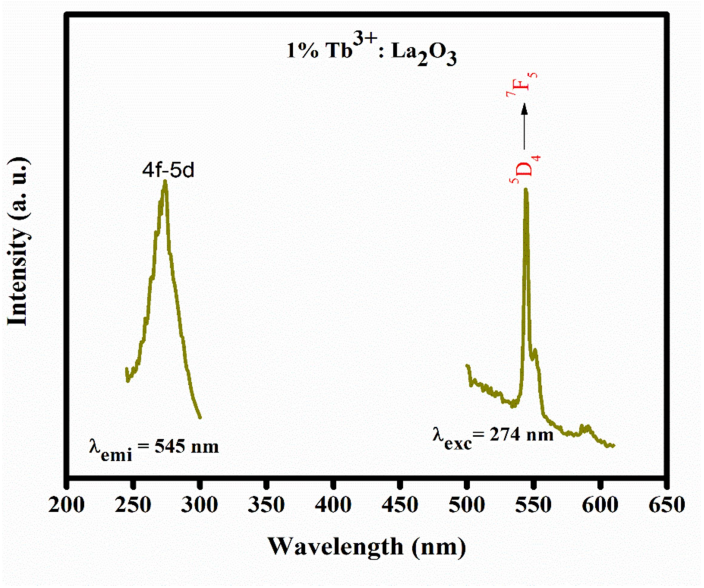

Figure 2.6 (c) Excitation & Emission characteristics of 1%Tb^{3+}: La_2O_3

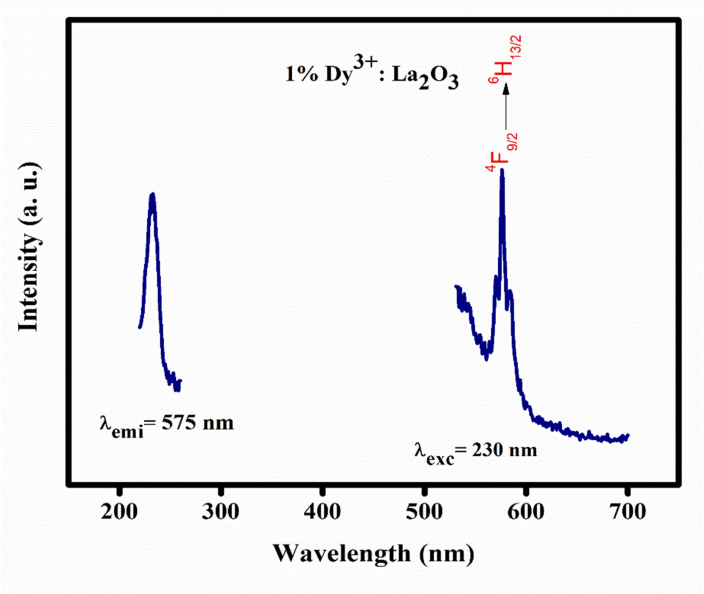

Figure 2.6 (d) Excitation & Emission characteristics of 1%Dy^{3+}: La_2O_3

Fig. 2.6 (a) shows the excitation and emission spectra of 1% Pr^{3+}: La_2O_3. The excitation spectrum was recorded at an emission wavelength of 400 nm. The peak excitation wavelength is at 260 nm (38416 cm^{-1}). The excitation peak is ascribed to 4f → $5d^1$ transition for Pr^{3+} ion. This transition depends on the host lattice. The covalence and crystal field of the

host lattice environment has a greater effect on the energy level of the 5d shell. The $4f^{n-1}5d^1$ energy level, situated at 38461 cm^{-1} in La_2O_3 excitation spectrum, is the lowest for the Pr^{3+} ion.

The emission spectrum was recorded at an excitation wavelength of 260 nm. Seven emission bands were recorded at wavelengths 388 nm (25773 cm^{-1}), 437 nm (22883 cm^{-1}), 450 nm (22222 cm^{-1}), 469 nm (21321 cm^{-1}), 483 nm (20703 cm^{-1}), 493 nm (20283 cm^{-1}) and 512 nm (19531 cm^{-1}). The emission at 388 nm is attributed to the transition from $4f^l5d^1$ to $^3H_4$ (0 cm^{-1}), which is an allowed transition and shows broadening. The other six emission bands are weak and ascribed to a $4f^2 \rightarrow 4f^2$ transition, which is forbidden in nature. The emissions at the wavelength of 437 nm and 450 nm are due to the transition from $^3P_2$ (22883 cm^{-1}) to $^3H_4$. Emission at wavelengths 483 nm & 493 nm are ascribed to transition from $^3P_1$ (20703 cm^{-1}) to $^3H_4$. The emission at 469 nm and 512 nm is due to transition from $^1I_6$ (21321 cm^{-1}) to $^3H_4$ & from $^3P_0$ (19531 cm^{-1}) to $^3H_4$. Hence, the transition from $4f^l5d^1$ to $4f^2$ is the most dominant emission transition [32].

From the fig 2.6 (b) for 1% Eu^{3+}: La_2O_3, PL excitation peak was observed at 275 nm at the emission wavelength λ_{emi} = 625 nm. The CTS (charge transfer stage) transition is accountable for PL excitation spectra for Eu^{3+}: La_2O_3 in which transition between 2p orbital of O^{2-} and 4f orbital of Eu^{3+} occurs.

The Emission Spectra was recorded at an excitation wavelength of λ_{exc} = 275 nm. There were seven emission peaks, observed at a wavelengths 540 nm, 555 nm, 583 nm, 590 nm, 597 nm, 615 nm and 627 nm, all due to 4f-4f the transition. The transition of energy level $^5D_1$ to $^7F_1$ is responsible for emission at 540 nm & 555 nm. The $^5D_0 \rightarrow {}^7F_0$ transition is responsible for emission at wavelength of 583 nm. Peaks at 590 nm and 597 nm are due to $^5D_0 \rightarrow {}^7F_1$. The emission at wavelengths of 615 nm and 627 nm are due to the transition between $^5D_0 \rightarrow {}^7F_2$ [32].

From fig 2.6 (c), Tb^{3+}: La_2O_3, the maximum excitation was observed at a wavelength of 274 nm for the emission wavelength λ_{emi} of 545 nm. The 4f→5d transition in Tb^{3+}: La_2O_3 is accountable for the excitation spectra. Under the excitation of 274 nm, one emission peak was observed. The transition between $^5D_4 \rightarrow {}^7F_5$ is responsible for a highest peak at 545 nm [32]. As shown in fig 2.6 (d) for Dy^{3+}: La_2O_3, the excitation was recorded at an emission wavelength of 575 nm. The excitation was maximum at a wavelength of 230 nm. The host absorption is accountable for excitation in 1% Dy^{3+}: La_2O_3. Under the excitation of 230 nm, the highest intensity peak was observed at 575 nm, which is due to the $^4F_{9/2} \rightarrow {}^6H_{13/2}$ transition [32].

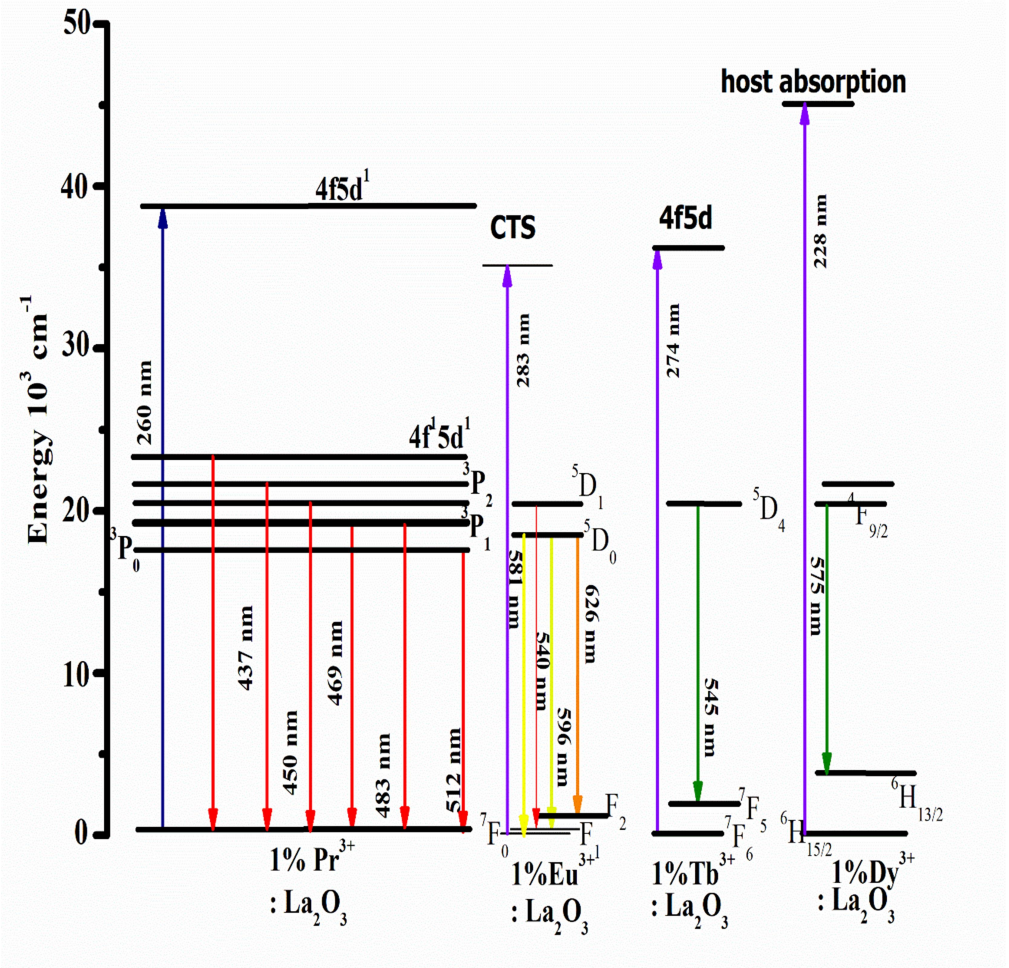

Figure 2.7 Energy level diagrams for down conversion photoluminescence

2.4 Results and Analysis for upconversion Samples:

2.4.1 Structural analysis:

A Rigaku SmartLab diffractometer operating at 30 mA, 40 kV was used for XRD characterization. The 2θ range scan was from 10 to 90°, with the step of 0.02°. The wavelength was 1.54 A° corresponding to Cu K_α radiation.

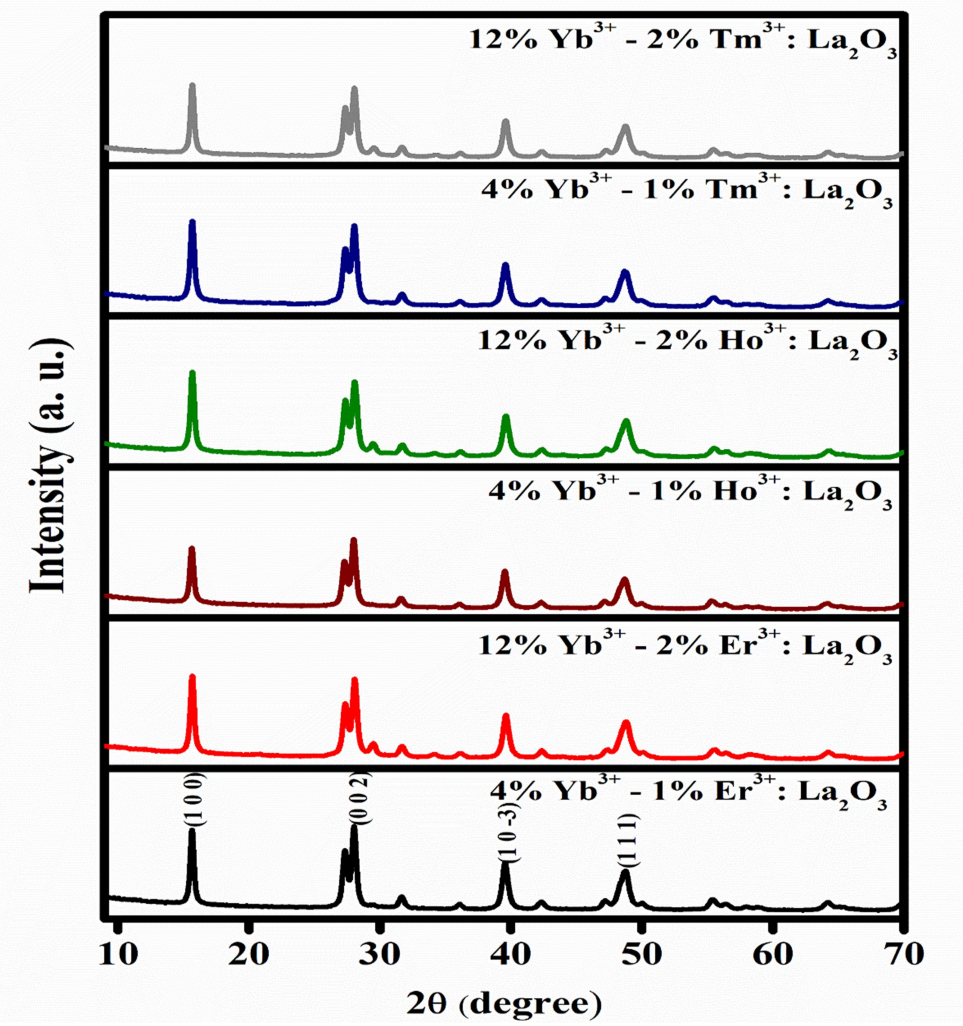

Figure 2.8 XRD of upconversion samples

Synthesized Materials	Phase Name with Space Group	Matching JCPDS file no.	Avg. Crystallite Size (nm)	Lattice Parameters (A°)			Volume $(A°)^3$
				a	b	c	
4% Yb^{3+}- 1% Er^{3+}: La_2O_3	Hexagonal $P\bar{6}2m$	83-1344, 83-1345, 40-1279, 40-1281	19.63	6.267	6.267	3.234	109.86
12% Yb^{3+}- 2% Er^{3+}: La_2O_3			18.56				
4% Yb^{3+}- 1% Ho^{3+}: La_2O_3			18.45				
12% Yb^{3+}- 2% Ho^{3+}: La_2O_3			17.22				
4% Yb^{3+}- 1% Tm^{3+}: La_2O_3			16.77				
12% Yb^{3+}- 2% Tm^{3+}: La_2O_3			12.14				

Table 2.4 Structural data of doped La_2O_3 samples extracted from the XRD spectra

2.4.2 Upconversion Photoluminescence analysis:

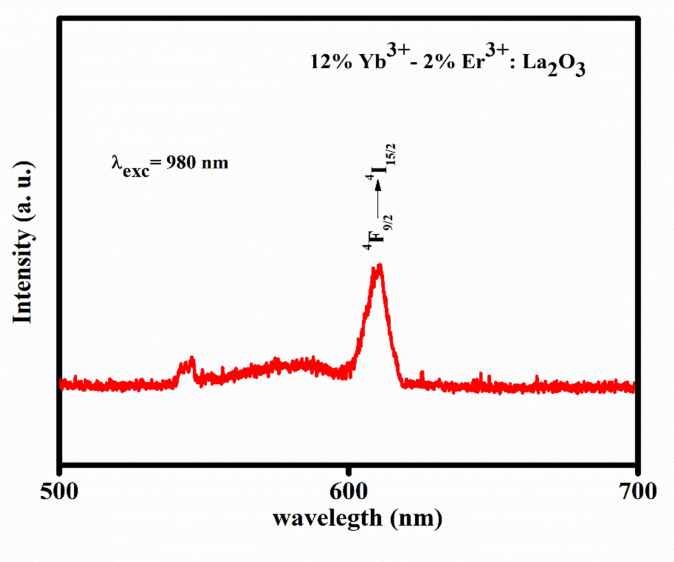

Figure 2.9 (a) Excitation & Emission characteristics of 12%Yb^{3+}-2%Er: La_2O_3

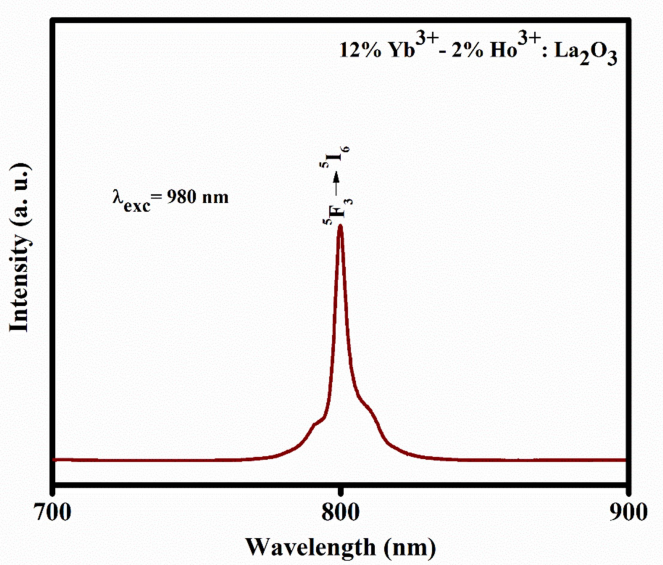

Figure 2.9 (b) Excitation & Emission characteristics of 12%Yb^{3+}-2%Ho: La_2O_3

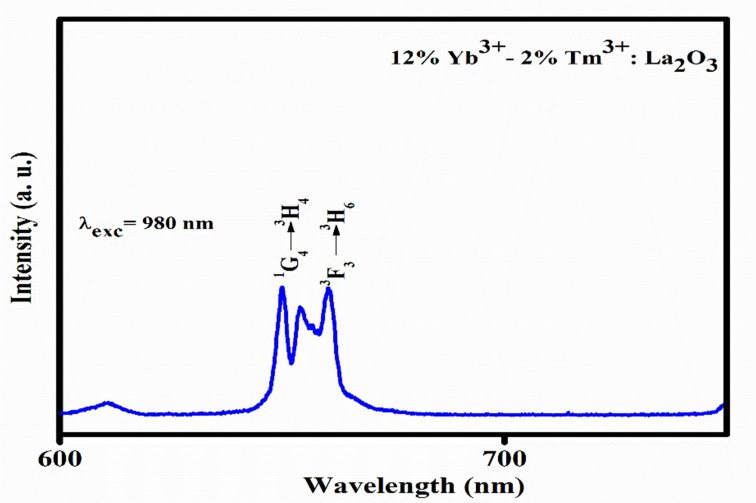

Figure 2.9 (c) Excitation & Emission characteristics of 12%Yb^{3+}-2%Tm: La_2O_3

For upconversion characteristics, the emission was recorded on a Horiba Jobin-Yvon model FHR 1000 Spectrophotometer with the fiber-optic bundle coupled to the high-resolution spectrograph having ICCD detector. Out of the six samples, only three samples show upconversion photoluminescence properties. The emission characteristics of all samples were recorded under 980 nm excitation.

The fig 2.9 (a) showing PL upconversion spectrum of 12%Yb^{3+}- 2%Er^{3+}: La_2O_3 has only one peak, which is observed at 610 nm and is attributed to $^4F_{9/2} \rightarrow {}^4I_{15/2}$ [32].

Fig. 2.9 (b) showing PL upconversion spectrum of 12%Yb^{3+}- 2%Ho^{3+}: La_2O_3 again shows a single peak at 800 nm, attributed to $^5F_3 \rightarrow {}^5I_6$ transition [32].

The PL upconversion spectrum of 12%Yb^{3+}- 2%Tm^{3+}: La_2O_3 in fig 2.9 (c) exhibits two peaks at wavelength of 650 nm & at 660 nm corresponding to the transitions $^1G_4 \rightarrow {}^3F_4$ and $^3F_2 \rightarrow {}^3H_6$ respectively [32].

The GSA (Ground State Absorption) and ETU (Energy Transfer Upconversion), both mechanisms are helpful to understand the upconversion process.

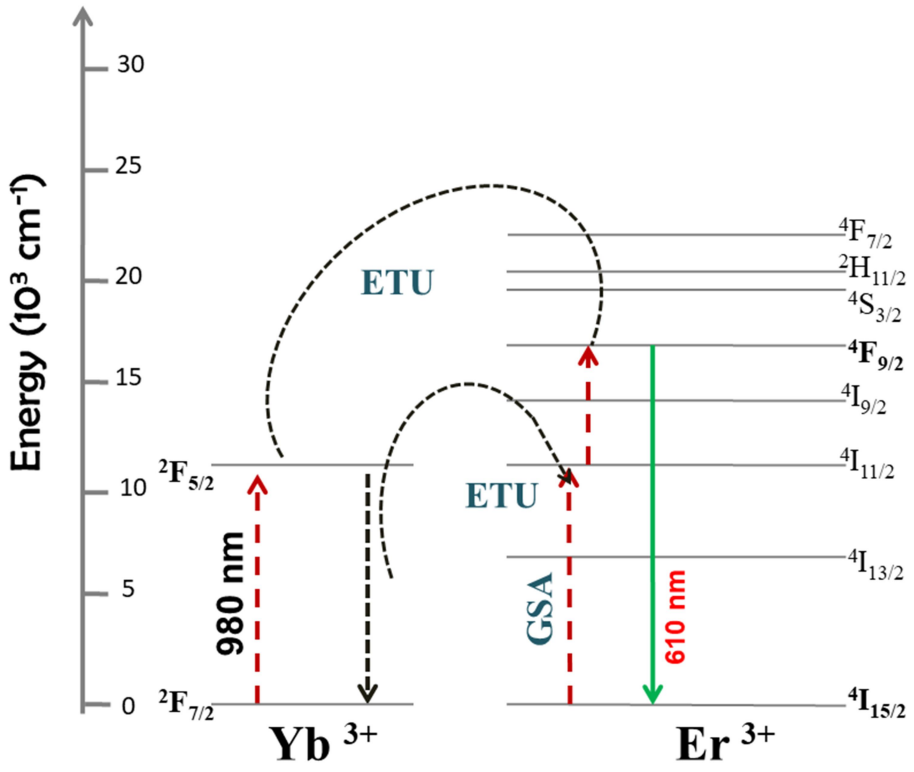

Figure 2.10 (a) Energy level diagram for Upconversion photoluminescence of 12%Yb^{3+}- 2%Er^{3+}: La_2O_3

As shown in Fig. 2.10 (a), the excitation energy at 980 nm is absorbed by the Yb^{3+} as well as Er^{3+} ions. The Yb^{3+} ions and Er^{3+} ions have the same energy for the first excited state (10204 cm^{-1}). The excitation results into transitions from $^2F_{7/2} \rightarrow {}^2F_{5/2}$ levels in Yb^{3+} ions and from $^4I_{15/2} \rightarrow {}^4I_{11/2}$ levels in Er^{3+} ions. Thus both the ions undergo Ground State Absorption. The energy emitted by the Yb^{3+} ions while returning to the ground state is transferred to the Er^{3+} ions, due to which they are propelled to energy level $^4F_{9/2}$ of Er^{3+}. The decay from $^4F_{9/2}$ to $^4I_{15/2}$ level in Er^{3+} ions results in emission.

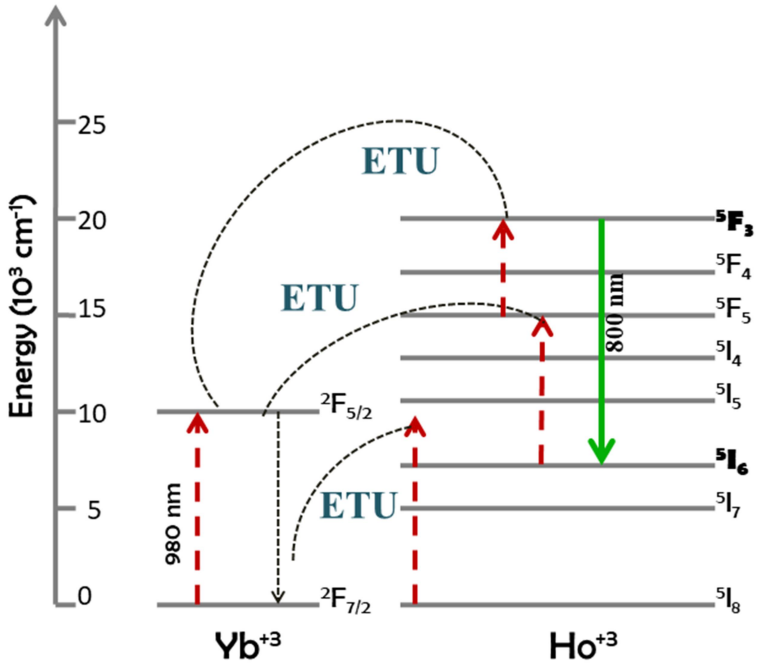

Figure 2.10 (b) Energy level diagram for Upconversion photoluminescence of 12%Yb^{3+}-2%Ho^{3+}: La_2O_3

As shown in fig 2.10 (b), the excitation at 980 nm is absorbed by only Yb^{3+} ions. This ground state absorption results into the transition $^2F_{7/2} \rightarrow {}^2F_{5/2}$ and subsequent emission from

$^2F_{5/2} \rightarrow {}^2F_{7/2}$. The emitted energy triggers the ground state absorption of Ho^{3+} ions from $^5I_8$. The emitted energy from Yb^{3+} ions further excites the Ho^{3+} ions at $^5I_6$ to $^5F_5$. The energy transfer is repeated again to take the Ho^{3+} ions from $^5F_5$ to $^5F_3$ energy levels which are the highest excited state in this case. The emission of 800 nm is attributed to the transition of Ho^{3+} ions from $^5F_3 \rightarrow {}^5I_6$.

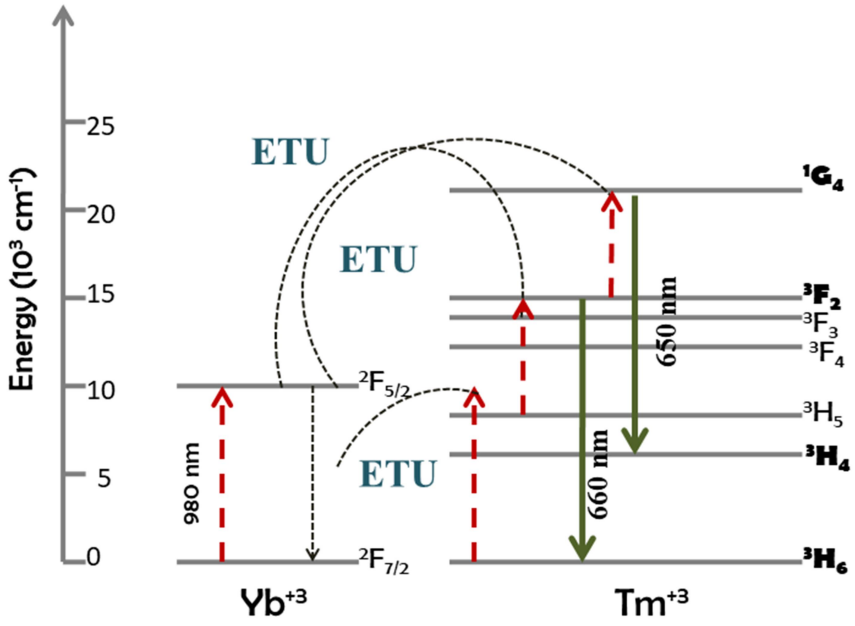

Figure 2.10 (c) Energy level diagram for Upconversion photoluminescence of 12%Yb^{3+}-2%Tm^{3+}: La_2O_3

As shown in fig 2.10 (c), the excitation at 980 nm is absorbed by only Yb^{3+} ions. This ground state absorption results into the transition $^2F_{7/2} \rightarrow {}^2F_{5/2}$ and subsequent emission from $^2F_{5/2} \rightarrow {}^2F_{7/2}$. The emitted energy triggers the ground state absorption of Tm^{3+} ions from $^3H_6$. The emitted energy from Yb^{3+} ions further excites the Tm^{3+} ions at $^3H_5$ to $^3F_2$. The emission

of 660 nm is attributed to the transition of Tm^{3+} ions from $^3F_2 \rightarrow {}^3H_6$. The energy transfer from Yb^{3+} ions results into another transition of from the $^3F_2$ to $^1G_4$ energy level, which is then de-excited to $^3H_4$ level by releasing the photon of 650 nm wavelength.

2.5 Conclusion:

The Nano Particles of the Lanthanum Oxide and 1%Ln^{3+}: La_2O_3 were successfully synthesized by aloe vera gel assisted precipitation method. The structural, elemental and optical properties were confirmed by the XRD, EDAX, UV-Visible and Photoluminescence spectrum respectively. The average sizes of synthesized particles were 55 nm with spherical shape was confirmed by SEM analysis.

References:

[1] L. Yu, Y. Han, R. Lin, K. Ge, C. Zhang, J. Zhang, G. Jia, Controllable synthesis and luminescence properties of one-dimensional La2O3 and La2O3:Ln3+ (Ln = Er, Eu, Tb) nanorods with different aspect ratios, J. Lumin. 229 (2021) 117663. doi:10.1016/j.jlumin.2020.117663.

[2] G. Maheshwaran, R. Selva Muneeswari, A. Nivedhitha Bharathi, M. Krishna Kumar, S. Sudhahar, Eco-friendly synthesis of lanthanum oxide nanoparticles by Eucalyptus globulus leaf extracts for effective biomedical applications, Mater. Lett. 283 (2021) 128799. doi:10.1016/j.matlet.2020.128799.

[3] M. Xue, M. Wei, H. Sheng, D. Bai, J. Wang, Tunable electronic properties of silicene based heterojunctions with ultrathin high-κ La2O3 gate dielectric, Superlattices

Microstruct. 147 (2020) 106686. doi:10.1016/j.spmi.2020.106686.

[4] S. Li, Y. Lin, Y. wu, Y. Wu, X. Li, W. Tian, Ni doping significantly improves dielectric properties of La2O3 films, J. Alloys Compd. 822 (2020) 2–11. doi:10.1016/j.jallcom.2019.153469.

[5] B. Sharma, A. Thapa, A. Sarkar, Ab-initio study of LD-HfO2, Al2O3, La2O3 and h-BN for application as dielectrics in MTJ memory device, Superlattices Microstruct. 150 (2021) 106753. doi:10.1016/j.spmi.2020.106753.

[6] N. Wang, X. Zhang, Z. Bai, Fabrication of highly transparent Er3+, Yb3+:Y2O3 ceramics with La2O3/ZrO2 as sintering additives and the near-infrared and upconversion luminescence properties, J. Alloys Compd. 842 (2020) 155932. doi:10.1016/j.jallcom.2020.155932.

[7] X. Huang, D. Zhao, L. Ma, C. Deng, L. Li, K. Chen, X. Yang, Effect of La2O3 on crystallization of Glass-ceramics, J. Non. Cryst. Solids. 536 (2020). doi:10.1016/j.jnoncrysol.2020.120007.

[8] R. Kurtulus, T. Kavas, I. Akkurt, K. Gunoglu, Theoretical and experimental gamma-rays attenuation characteristics of waste soda-lime glass doped with La2O3 and Gd2O3, Ceram. Int. 47 (2021) 8424–8432. doi:10.1016/j.ceramint.2020.11.207.

[9] J. Zhang, Z. Zhang, Y. Jiao, H. Yang, Y. Li, J. Zhang, P. Gao, The graphene/lanthanum oxide nanocomposites as electrode materials of supercapacitors, J. Power Sources. 419 (2019) 99–105. doi:10.1016/j.jpowsour.2019.02.059.

[10] H.C. Swart, R.E. Kroon, Ultraviolet and visible luminescence from bismuth doped materials, Opt. Mater. X. 2 (2019) 100025. doi:10.1016/j.omx.2019.100025.

[11] G. Sharma, A. Kumar, S. Sharma, S.I. Al-Saeedi, G.M. Al-Senani, A. Nafady, T. Ahamad, M. Naushad, F.J. Stadler, Fabrication of oxidized graphite supported La 2 O 3 /ZrO 2 nanocomposite for the photoremediation of toxic fast green dye, J. Mol. Liq. 277 (2019) 738–748. doi:10.1016/j.molliq.2018.12.126.

[12] L. Yue, F. Chen, K. Yu, Z. Xiao, X. Yu, Z. Wang, B. Xing, Early development of apoplastic barriers and molecular mechanisms in juvenile maize roots in response to La 2 O 3 nanoparticles, Sci. Total Environ. 653 (2019) 675–683. doi:10.1016/j.scitotenv.2018.10.320.

[13] P. Liu, Y. Cui, G. Gong, X. Du, J. Wang, X. Gao, M. Jia, J. Yu, Vanadium contamination on the stability of zeolite USY and efficient passivation by La2O3 for cracking of residue oil, Microporous Mesoporous Mater. 279 (2019) 345–351. doi:10.1016/j.micromeso.2019.01.023.

[14] B.M. Jaffar, H.C. Swart, H.A.A. Seed Ahmed, A. Yousif, R.E. Kroon, Luminescence properties of Bi doped La 2 O 3 powder phosphor, J. Lumin. 209 (2019) 217–224. doi:10.1016/j.jlumin.2019.01.044.

[15] A. Huminic, G. Huminic, C. Fleacă, F. Dumitrache, I. Morjan, Thermo-physical properties of water based lanthanum oxide nanofluid. An experimental study, J. Mol. Liq. 287 (2019). doi:10.1016/j.molliq.2019.111013.

[16] M.U. Azam, M. Tahir, M. Umer, M.M. Jaffar, M.G.M. Nawawi, Engineering approach to enhance photocatalytic water splitting for dynamic H2 production using La2O3/TiO2 nanocatalyst in a monolith photoreactor, Appl. Surf. Sci. 484 (2019) 1089–1101. doi:10.1016/j.apsusc.2019.04.030.

[17] A. Umar, A.A. Ibrahim, R. Kumar, T. Almas, P. Sandal, M.S. Al-Assiri, M.H.

Mahnashi, B.Z. AlFarhan, S. Baskoutas, Fern shaped La2O3 nanostructures as potential scaffold for efficient hydroquinone chemical sensing application, Ceram. Int. 46 (2020) 5141–5148. doi:10.1016/j.ceramint.2019.10.258.

[18] G. Cabello-Guzmán, C. Caro-Díaz, A. Fernandez-Perez, G.E. Buono-Core, B. Chornik, Study of the influence of Er/Ln co-doping in La2O3 thin films on their up-conversion properties (where Ln = Ho or Nd), Opt. Mater. (Amst). 99 (2020). doi:10.1016/j.optmat.2019.109579.

[19] N. Jain, R.K. Singh, A. Srivastava, S.K. Mishra, J. Singh, Prominent blue emission through Tb3+ doped La2O3 nano-phosphors for white LEDs, Phys. B Condens. Matter. 538 (2018) 70–73. doi:10.1016/j.physb.2018.03.014.

[20] G. Chen, R. Lei, S. Xu, H. Wang, S. Zhao, F. Huang, Y. Tian, Effect of Li+ ion concentration on upconversion emission and temperature sensing behavior of La2O3:Er3+ phosphors, J. Rare Earths. 36 (2018) 119–124. doi:10.1016/j.jre.2017.03.004.

[21] Y. Zhang, W. Li, T. Zhang, B. Yang, Q. Zheng, J. Xu, H. Wang, L. Wang, X. Zhang, B. Wei, The feasibility of using solution-processed aqueous La2O3 as effective hole injection layer in organic light-emitting diode, Solid. State. Electron. 139 (2018) 54–59. doi:10.1016/j.sse.2017.10.036.

[22] Z. Sun, G. Liu, Z. Fu, T. Sheng, Y. Wei, Z. Wu, Nanostructured La2O3: Yb3+/Er3+: Temperature sensing, optical heating and bio-imaging application, Mater. Res. Bull. 92 (2017) 39–45. doi:10.1016/j.materresbull.2017.04.005.

[23] A. Siaï, P. Haro-González, K. Horchani-Naifer, M. Férid, La2O3: Tm, Yb, Er upconverting nano-oxides for sub-tissue lifetime thermal sensing, Sensors Actuators, B

Chem. 234 (2016) 541–548. doi:10.1016/j.snb.2016.05.019.

[24] P.V.S.S.S.N. Reddy, D. Narendra Babu, G.M.M. Kishore, S. V. Naveen, B. V. Ramana, B. Srinivas, B. V. Naveen, K. Ramachandra Rao, C. Satya Kamal, Polyol derived Bi3+ and Er3+ co-doped lanthanum oxide nanophosphors for display & LED applications, Mater. Today Proc. 18 (2019) 2118–2122. doi:10.1016/j.matpr.2019.06.485.

[25] M. Veerasingam, B. Murugesan, S. Mahalingam, Ionic liquid mediated morphologically improved lanthanum oxide nanoparticles by Andrographis paniculata leaves extract and its biomedical applications, J. Rare Earths. 38 (2020) 281–291. doi:10.1016/j.jre.2019.06.006.

[26] F. V. Molefe, L.L. Noto, M.S. Dhlamini, B.M. Mothudi, V.R. Orante-Barrón, Structural, photoluminescence and thermoluminescence study of novel Li+ co-activated lanthanum oxide activated with Dy3+ and Eu3+ obtained by microwave-assisted solution combustion synthesis, Opt. Mater. (Amst). 88 (2019) 540–550. doi:10.1016/j.optmat.2018.12.025.

[27] S. Karthikeyan, M. Selvapandiyan, S. Shanavas, P.M. Anbarasan, R. Acevedo, A role of annealing temperature on the properties of lanthanum oxide (La2O3) microplates by reflux routes, Mater. Today Proc. 26 (2019) 3576–3578. doi:10.1016/j.matpr.2019.07.700.

[28] B.P. Gangwar, S. Irusta, S. Sharma, Physicochemical and optical properties of one-pot combustion synthesized Pr doped La2O3/La(OH)3, J. Lumin. 219 (2020). doi:10.1016/j.jlumin.2019.116893.

[29] G. Gao, L. Yang, B. Dai, F. Xia, Z. Yang, S. Guo, P. Wang, F. Geng, J. Han, J. Zhu,

Investigation of the effect of annealing temperature on optical properties of lanthanum-oxide thin films prepared by sol-gel method, Surf. Coatings Technol. 365 (2019) 164–172. doi:10.1016/j.surfcoat.2018.07.001.

[30] J. Tauc, R. Grigorovici, A. Vancu, Optical Properties and Electronic Structure of Amorphous Germanium, Phys. Status Solidi. (1966). doi:10.1002/pssb.19660150224.

[31] V. Kumar, J.K. Singh, Model for calculating the refractive index of different materials, Indian J. Pure Appl. Phys. (2010).

[32] G.H. Dieke, H.M. Crosswhite, B. Dunn, Emission Spectra of the Doubly and Triply Ionized Rare Earths*, J. Opt. Soc. Am. 51 (1961) 820. doi:10.1364/josa.51.000820.